Earth Syst. Sci. Data, 18, 8971–8988, 2026
https://doi.org/10.5194/essd-18-8971-2026
© Author(s) 2026. This work is distributed under
the Creative Commons Attribution 4.0 License.

Open Access Earth System Science Data

Spectral correction factors for the removal of glint perturbations in above-water radiometry

Barbara Bulgarelli[1], Davide D'Alimonte[2], Giuseppe Zibordi[3,4], and Tamito Kajiyama[2]

[1]European Commission, Joint Research Centre (JRC), Ispra, Italy
[2]Aequora, Lisbon, Portugal
[3]National Aeronautics and Space Administration, Goddard Space Flight Center, Greenbelt, MD 20771, USA
[4]Southeastern Universities Research Association, Washington, DC 20005, USA

Correspondence: Barbara Bulgarelli (barbara.bulgarelli@ec.europa.eu)

Received: 16 June 2026 – Discussion started: 13 July 2026
Revised: 14 October 2026 – Accepted: 22 October 2026 – Published: 27 November 2026

Abstract. Spectral correction factors for the removal of glint perturbations in above-water radiometric measurements are theoretically computed for representative inland, coastal and open-ocean waters, accounting for atmospheric dependences. The simulation framework relies on the measurement protocol adopted by AERONET-OC and endorsed by the ocean color community to support the validation of satellite aquatic radiometric products. The theoretical computation of the correction factors, here termed *glint correction factors* or *ρ-factors*, is performed in the 340–1020 nm spectral range by coupling (i) a highly accurate plane-parallel scalar code to simulate the angular distribution of the spectral sky-radiance impinging at the water surface, with (ii) a three-dimensional Monte Carlo code to model radiance reflections at a wind-roughened water surface. Glint is conventionally distinguished into contributions from radiance originating in the sun region (sun-glint) and in the remaining portion of the sky-dome (sky-glint); the impact of these terms is separately discussed. Computed glint correction factors – for both the total sky radiance and its sole diffuse component – are available at Zenodo (Bulgarelli et al., 2026; https://doi.org/10.5281/zenodo.20609990).

1 Introduction

The primary data product of aquatic optical remote sensing is the light emerging from the water, the so-called water-leaving radiance L_w (a summary of the mathematical notation used throughout the manuscript is provided in Appendix A). This carries information on the water optically significant components, such as the concentration of pigmented particles, which is a proxy for phytoplankton biomass.

While L_w only accounts for a small fraction of the total signal at the satellite sensor, its application in environmental and climate investigations requires a high level of accuracy.

Pivotal to the fulfillment of these accuracy requirements is the validation of satellite data products through comparison with in situ reference measurements.

Among the different methodologies established to acquire accurate in situ measurements of L_w, above-water radiometry relies on optical instruments deployed from ships or fixed platforms (Zibordi and Voss, 2014), and more recently from unmanned aerial vehicles (Sciuto et al., 2026).

Radiometric measurements performed from above the water are perturbed by the sky radiance reflected by the water surface (the *glint*), distinguished into glint from radiance originating in the sun region (*sun-glint*) and glint from radiance originating in the remaining portion of the sky-dome (*sky-glint*). These perturbations must be removed to determine the target signal L_w.

The protocols commonly applied to determine L_w from above-water measurements require acquisitions of the total radiance from the water L_T in direction θ and ϕ, and of the sky radiance L_i in the direction specular to L_T (i.e., in direction $\theta' = 180° - \theta$ and ϕ). The angle of observation θ is measured with respect to nadir, while the azimuth ϕ indicates the relative angle between the solar and the measurement planes

(see Fig. 1). Recommendations for ϕ and θ maximizing the accuracy of glint corrections are provided in Mobley (1999) and IOCCG (2019).

The water-leaving radiance L_w at wavelength λ is derived by removing from L_T the radiance L_R reflected by the water surface, which is assumed proportional to L_i:

$$L_w(\theta,\phi,\lambda) = L_T(\theta,\phi,\lambda) - L_R(\theta,\phi,\lambda) = L_T(\theta,\phi,\lambda) - \rho(\theta,\phi,\lambda)\cdot L_i(\theta',\phi,\lambda). \quad (1)$$

The proportionality factor ρ is here termed the *glint correction factor*. This term is preferred to previously used designations (*sea-surface reflectance factors* or *surface-to-sky radiance ratios*) to acknowledge that: (i) ρ is not a proper reflectance; (ii) the correction applies to any water surface (not only marine); and finally, (iii) to highlight its operational scope to remove glint perturbations affecting above-water radiometric measurements.

In addition to wavelength and viewing geometry, ρ depends on the sun zenith angle θ_0, the wind speed v_w, and the atmospheric optical properties expressed by the aerosol type and the aerosol optical depth τ_a, which were omitted in Eq. (1) for simplicity of notation. For a flat water surface and an infinitesimal sensor field-of-view (FOV), ρ would become the Fresnel reflectance and L_R would be entirely determined by the specular reflection of L_i. For a wind-roughened water surface observed over a finite time-window by a sensor with a finite FOV, each surface facet would still obey Fresnel's law, but the wind-driven distribution of facet slopes would cause L_R to be determined by reflections of radiance originating from a broader region of the sky-dome around the specular direction (θ',ϕ). The glint correction factor ρ accounts for the roughness of the water surface and for the angular distribution of sky radiance, and is theoretically computed according to:

$$\rho(\theta,\phi,\lambda) = \frac{L_R(\theta,\phi,\lambda)}{L_{sky}(\theta',\phi,\lambda)}, \quad (2a)$$

where the radiance $L_R(\theta,\phi,\lambda)$ reflected by the water surface in direction (θ,ϕ) is given by

$$L_R(\theta,\phi,\lambda) = \int_0^{2\pi}\int_0^{\pi/2} L_{sky}(\theta^*,\phi^*,\lambda) \cdot r(\theta^*,\phi^* \to \theta,\phi;\ \lambda;\ v_w)\sin\theta^*\, d\theta^*\, d\phi^*. \quad (2b)$$

In this expression, $r(\theta^*,\phi^* \to \theta,\phi;\ \lambda;\ v_w)\sin\theta^*$ indicates the probability density that the sky radiance L_{sky} impinging from direction (θ^*,ϕ^*) on a water surface roughened by wind speed v_w is reflected in the direction (θ,ϕ). Term L_{sky} may include both the direct and diffuse components, and the integration is performed over the whole sky-dome. Term $L_{sky}(\theta',\phi,\lambda)$ in the denominator is the theoretical quantification of the measured quantity $L_i(\theta',\phi,\lambda)$.

In the following, ρ-factors accounting for both direct and diffuse (i.e., total) L_{sky} will be denoted by ρ_T, while ρ-factors accounting for the sole diffuse sky-radiance will be denoted by ρ_d.

Terms L_{sky}, r, ρ_d and ρ_T are computed via radiative transfer simulations.

Glint correction factors regularly utilized by the scientific community in the processing of above-water radiometric data were computed by Mobley (1999) using the scalar Hydrolight code (Mobley, 1994) accounting for both direct and diffuse sky-radiance contributions. The sky radiance was simulated at $\lambda = 550$ nm according to Harrison and Coombes (1988) and assuming a fixed aerosol optical depth $\tau_a^{550} = 0.26$ (D'Alimonte et al., 2021). The wave-slope distribution was modeled according to Cox and Munk (1954), neglecting the constant background term. The same author subsequently provided vectorial simulations of ρ_T at the same wavelength (Mobley, 2015) by assuming a pure molecular atmosphere and by modelling the wave-slope distribution according to Elfouhaily et al. (1997). An experimental evaluation of the impact on above-water data products of these two sets of ρ_T values, restricted to θ_0 larger than 20° and to wind v_w generally lower than $5\,m\,s^{-1}$, indicated slightly better performance of the scalar factors accounting for aerosols and multiple scattering than the vectorial ones computed under a pure molecular atmosphere (Zibordi, 2016).

Experimental evidence of the spectral dependence of ρ (Lee et al., 2010) motivated investigations into alternative ρ-factors.

Zhang et al. (2017) applied a Monte Carlo simulation framework with spectrally explicit sky-radiance distributions, separating sky-glint from sun-glint contributions. The study showed that the spectral dependence of ρ_T exhibits a slight decrease with wavelength at low wind speeds and conversely a marked increase with wavelength for high wind speeds and low solar zenith angles. This behavior is primarily driven by the spectral distribution of skylight, with a minor contribution from the spectral dependence of the water refractive index. Simulations were performed over the 350–1000 nm range adopting a MODerate resolution atmospheric TRANsmission (MODTRAN; Berk et al., 2006) atmosphere with maritime aerosol and $\tau_a^{550} = 0$, 0.05, 0.1 and 0.3. A vector radiative transfer model was additionally applied to perform an exploratory investigation of the impact of polarization, suggesting a moderate increase of sky-glint in the blue.

Gilerson et al. (2018) applied a one-dimensional vector radiative transfer code to simulate ρ_T factors in the 400–900 nm spectral range for oceanic and partially continental aerosols with τ_a^{440} ranging from 0 to 1.0, demonstrating a significant impact of aerosol optical depth and type on the spectral values of ρ_T.

Harmel (2023) applied the vectorial plane-parallel Ordres Successifs Océan Atmosphère Avancé code (OSOAA; Chami et al., 2015) to compute ρ_d factors between 350 and 1000 nm for OPAC (Optical Properties of Aerosols and

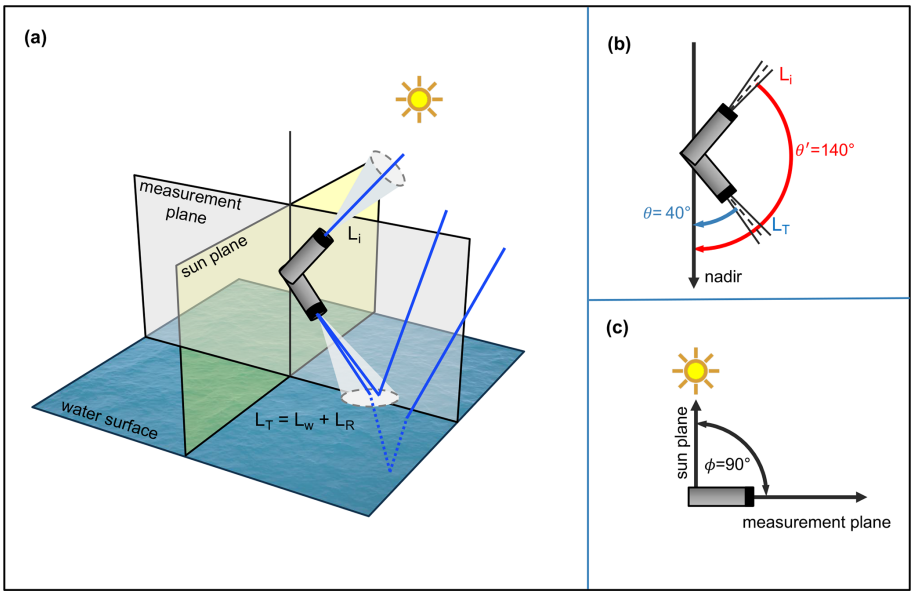


Figure 1. **(a)** Typical above-water measurement geometry. **(b)** Side- and **(c)** top-view measurement geometry applied to AERONET-OC and supported by current protocols.

Clouds; Hess et al., 1998) pure maritime, continental, desert dust and urban polluted aerosols, with τ_a^{550} from 0 to 1.5.

The authors of the present work proposed scalar ρ_T factors (D'Alimonte et al., 2021; Bulgarelli et al., 2022, 2024) accounting for spectral and atmospheric dependences obtained by coupling the scalar plane-parallel Finite Element Method radiative transfer code (FEM; Bulgarelli et al., 1999; Kisselev et al., 1995) with the three-dimensional Monte Carlo for Ocean Color Simulation code (MOX; D'Alimonte et al., 2010, 2021; Kajiyama et al., 2016). This development, which specifically refers to the measurement protocol applied by the Ocean Color component of the Aerosol Robotic Network (AERONET-OC; Zibordi et al., 2009, 2021), adopted pure and mixed continental and maritime aerosols from the OPAC database with τ_a^{500} ranging between 0 and 0.5.

A comparison of these ρ_T factors with those of Mobley (1999) is provided in D'Alimonte et al. (2021) and further analyzed in Bulgarelli et al. (2024).

Utilizing the same simulation framework, and acknowledging that AERONET-OC data processing applies a threshold to the standard deviation of the L_T distribution to remove measurement sequences affected by appreciable sun-glint contamination (Zibordi et al., 2022), ρ_d factors were computed to support investigations into the impact of alternative processing on AERONET-OC data (Zibordi et al., 2025). The study, which compared diverse solutions alternatively relying on ρ_T from Mobley (1999), ρ_d from FEM-MOX and ρ_d from Harmel (2023) (see Fig. 1 of Zibordi et al., 2025), indicated a slightly better agreement with independent field reference measurements when scalar ρ_d from FEM-MOX are applied with respect to ρ_d from Harmel (2023) accounting for polarization.

This result supported the application of FEM-MOX scalar ρ_d factors in the forthcoming AERONET-OC Version 4 processing, and additionally as optional glint correction factors in the HyperCP community processor (Tilstone et al., 2025), thus motivating their public access.

Building on previous investigations on ρ_T (Bulgarelli et al., 2024), the present study advances in several directions. First, the atmospheric model is updated to provide a more realistic representation of aerosol and gas molecules. Second, values of $\rho_D = \rho_T - \rho_d$ are used to investigate sun-glint contamination under diverse measurement conditions. Third, and most importantly, the ρ_d factors are formally presented and discussed, together with updated ρ_T values.

Newly simulated values of ρ_T and ρ_d are made available at Zenodo for typical observation conditions in inland, coastal and open-ocean regions, for the specific AERONET-OC measurement geometry (namely $\theta = 40°$ and $\phi = 90°$, as in Fig. 1b and c) supported by the IOCCG protocols (IOCCG, 2019). It is underlined that measurements performed with alternative larger azimuth angles (e.g., $\phi = 135°$) can be impacted by perturbations from the deployment platform such as fixed structures or ships, with errors in derived data products difficult to quantify without dedicated investigations (D'Alimonte et al., 2026).

The methodology applied is described in Sect. 2, while results are illustrated and discussed in Sect. 3. A detailed description of the dataset comprising the ρ_T and ρ_d factors is given in Sect. 4. Conclusions are drawn in Sect. 5.

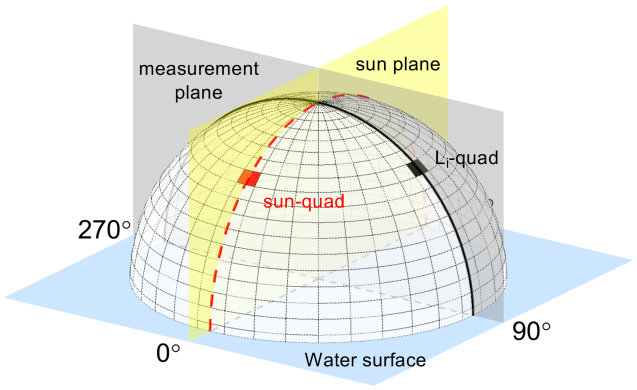


Figure 2. Partitioning of the sky-dome into quads. The black thick solid and red dashed lines indicate the measurement and the solar planes, respectively. The black L_i*-quad* encompasses the direction of L_i (which is specular to the down-looking direction of the virtual radiometer). The red *sun-quad* encompasses the sun position (θ_0, ϕ_0), while the solar plane is identified by ϕ_0 and $180° + \phi_0$; for convenience ϕ_0 is set to 0°.

2 Methodology

2.1 The simulation framework

For computational purposes, the sky-dome is divided into a discrete number of angular grid elements (hereafter named *quads*) of dimension $\Delta\theta_k \times \Delta\phi_m$ (for $k = 1, \ldots, N_\theta = 19$ and $m = 1, \ldots, N_\phi = 36$), so that Eq. (2) can be rewritten as:

$$\rho = \frac{\sum_{k}^{N_\theta}\sum_{m}^{N_\phi}\mathbf{R}(k,m)\cdot\mathbf{L}(k,m)}{\mathbf{L}(k_i,m_i)}. \quad (3)$$

In Eq. (3), $\mathbf{R}$ indicates the *water-surface reflectance matrix*, with $\mathbf{R}(k,m) = r(\theta_k, \phi_m \rightarrow \theta, \phi;\ \lambda;\ v_w)\sin\theta_k \Delta\theta_k \Delta\phi_m$; $\mathbf{L}$ the *sky-radiance matrix*, where $\mathbf{L}(k,m)$ corresponds to values of L_{sky} computed at the barycenter of the (k,m)-quad and rescaled to preserve diffuse and direct irradiances; and $\mathbf{L}(k_i,m_i)$ corresponds to the value of $\mathbf{L}$ at the quad encompassing $L_{sky}(\theta', \phi, \lambda)$ which simulates the experimentally measured sky-radiance L_i, and is hence hereafter referred to as the L_i*-quad* (see Fig. 2).

Term $\mathbf{L}$ is calculated with FEM in its SkyFEM configuration, while term $\mathbf{R}$ is computed with MOX.

FEM is a radiative transfer code (Bulgarelli et al., 1999; Kisselev et al., 1995) designed to simulate the propagation of unpolarized monochromatic radiation at ultraviolet, visible, and near-infrared wavelengths in a vertically inhomogeneous medium with one change in the refractive index (e.g., the atmosphere-water system). Comprehensively tested and benchmarked with various codes (Bulgarelli et al., 1999, 2003; Bulgarelli and Doyle, 2004), FEM applies the finite-element deterministic approach to solve the radiative transfer equation, fully accounting for multiple scattering, and reflection and refraction at the water surface. In its SkyFEM configuration, FEM is coupled with the PERSEA (Propagating Environment for Radiance Simulations in atmosphEre and wAter) code, allowing the generation of sky-radiance angular distributions for different atmospheric models, relying on existing parameterizations, external databases, or user-provided inputs (Bulgarelli, 2024).

MOX is a three-dimensional stochastic code developed to support investigations on in situ ocean color measurements (D'Alimonte et al., 2010; Kajiyama et al., 2016). The code can perform both forward and backward ray tracing. In the first case, equivalent to physical measurement conditions, rays are traced from the source in the sky-dome to the virtual radiometer. In the latter case, which is that adopted in the present study, rays are traced from the virtual radiometer back to the source. MOX fully accounts for the radiometer FOV and for multiple reflections at the water surface. The latter is defined over a square domain of side $L = 50$ m discretised in approximately 1000 intervals along the x- and y-axis. Each surface element is further split into two triangular elements whose vertices are elevated based on the adopted water-surface model (see Sect. 2.2). The reader is referred to D'Alimonte et al. (2021) for details.

2.2 Atmosphere and water surface modelling

Modelling is performed by assuming clear-sky conditions, using the spectral extra-terrestrial solar irradiance from Thuillier et al. (2003), and dividing the atmosphere, bounded by the water surface, into 32 plane-parallel layers to resolve the vertical distribution of aerosols and gas molecules. Since simulations solely target the sky-radiance impinging at the water surface, the water body is assumed totally absorbing.

The spectral properties and the vertical distribution of gas molecules are taken from the Air Force Geophysics Laboratory (AFGL) model (Anderson et al., 1986). The optical properties and vertical distribution of aerosols are taken from the OPAC software package (Hess et al., 1998), which models distinctive aerosol mixtures through the combination of ten individual components (e.g., soot, sea-salt, mineral, water-soluble, ...) at different relative humidity (RH), and which assumes three distinct aerosol layers – tropospheric, free-tropospheric and stratospheric. The optical properties of each aerosol mixture are theoretically calculated from the size distribution and the spectral refractive index of its reference optical components by applying the Mie theory under the assumption of spherical particles. Selected OPAC aerosol output parameters are the extinction coefficient, the single scattering albedo, the phase function asymmetry parameter, and the phase function at 112 scattering angles. The Ångström exponents (Ångström, 1961) $\alpha_{350-500}$, for the 350–500 nm range, and $\alpha_{500-800}$, for the 500–800 nm range, are also utilized.

Each aerosol phase function derived from the OPAC database is modeled using 1000 Legendre polynomials with-

out applying any truncation. Relative differences between original phase function values and those obtained through Legendre expansion never exceed ±11 % with a standard deviation of 1.5 ± 1.8 % across all models and all angles. Absolute percent differences in the integral between original and reconstructed phase functions never exceed 0.9 %.

Atmospheric modeling updates with respect to Bulgarelli et al. (2024) include the use of the AFGL model for the gas molecule properties and the inclusion of the free-tropospheric and stratospheric aerosol layers.

The water surface model accounts for the spectral dependence of the refractive index, and adopts the slope distribution of surface waves from Cox and Munk (1954) expressed as a Gaussian function with variance σ^2:

$$\sigma^2 = 0.003 + 0.00512 \cdot v_w \quad (4)$$

where the wind speed v_w is in units of $m\,s^{-1}$ and 0.003 is referred to as *the background term*.

2.3 Simulation cases and parameter space

Representative cases were selected to cover typical measurement conditions in inland, coastal and open-ocean regions (Table 1). These include the nominal center-wavelengths of relevance for AERONET-OC measurements; sun zenith angle θ_0 ranging between 10 and 80°; sun azimuth angle ϕ_0 set to 0° (this value is systematically applied across simulations as $\phi_0 \pm 90°$ is the relevant quantity defining the measurement geometry with respect to the illumination one); omnidirectional wind speed v_w varying between 0 and $10\,m\,s^{-1}$ in the absence of whitecaps or surface scums; total aerosol optical depth at 560 nm, τ_a^{560} in the 0.05–0.5 range; and three distinct OPAC tropospheric aerosol mixtures at RH = 80 % (Hess et al., 1998):

- Clean maritime aerosol (MA),
- A mix of 80 % average continental and 20 % clean maritime aerosols (MX),
- Polluted continental aerosol (CO).

The adoption of MA, MX and CO tropospheric aerosols yields a columnar Ångström exponent in the 440–870 nm interval $\alpha^{col}_{440\text{–}870} = -\log\left(\frac{\tau_a^{440}}{\tau_a^{870}}\right)/\log\left(\frac{440}{870}\right) = 0.19, 1.08, 1.42$ for $\tau_a^{560} = 0.2$, respectively, where τ_a^{λ} represents the columnar aerosol optical depth at λ. These values characterize a range of cases, spanning from open ocean to inland water environments, with the mixed model (MX) representative of coastal sites where marine and continental aerosol contributions are both significant.

Examples of the vertical profiles of the atmospheric inherent optical properties are shown in Fig. 3.

The selected atmospheric parameters were confirmed via comparison with (i) maritime aerosol occurrences in the open ocean (see Smirnov et al., 2009, and dedicated AERONET Maritime Aerosol Network (MAN) measurements) and (ii) field data from AERONET-OC sites (Zibordi et al., 2009) assumed representative of atmospheric optical conditions in both coastal and inland regions.

Multi-annual yearly averages of τ_a^{500} and $\alpha_{440\text{–}870}$ for representative AERONET-OC sites, as extracted from AERONET climatological Level 2.0 data (Holben et al., 1998), are displayed in Fig. 4. The average values with standard deviation across all the considered sites are $\tau_a^{500} = 0.18 \pm 0.09$, and $\alpha^{col}_{440\text{–}870} = 1.14 \pm 0.30$.

2.4 Computed quantities

Glint correction factors ρ were computed accounting for (see Eqs. 2 and 3):

- the total sky-radiance (ρ_T),
- the sole diffuse sky-radiance (ρ_d).

Overall, sky-radiance distributions were determined for 18 atmospheric cases at 22 center-wavelengths, assuming 8 different sun zenith angles for a total of 3168 sky-radiance angular distributions (at 684 discrete angles). The values of ρ_T and ρ_d were further computed for 6 different water surface conditions for a total of 19 008 values of each of ρ_T and ρ_d.

The sky radiance impinging on the water surface from the sun direction naturally contains both a direct and a diffuse component, where the latter corresponds to the narrow peak of forward-scattered direct sun radiance (see Figs. 5 and 6). As a consequence, any quality-control procedure to remove above-water radiometric measurements affected by sun-glint contamination would implicitly filter out contributions from the diffuse sky-radiance peak, too. Yet, simulations of ρ_d account for diffuse radiance contributions from the entire sky-dome, thus including this same peak. This potentially introduces an inconsistency when ρ_d is applied to above-water radiometric measurements filtered for sun-glint contamination. Still recognizing that in the adopted simulation framework the dimension of the quad containing the sun (*sun-quad*) is larger than the actual sun dimension, possible implications of discrepancies between operational and simulation frameworks have been analyzed by comparing the values of ρ_d with glint correction factors simulated by masking the sun-quad ($\rho_{\tilde{sq}}$).

Differences between $\rho_{\tilde{sq}}$ and ρ_d show percent values not exceeding −1.2 % across all measurement conditions, and decreasing to −0.02 % for cases characterizing AERONET-OC quality-controlled data performed in the 400–709 nm spectral interval (generally determined with $v_w \le 4\,m\,s^{-1}$ and $\theta_0 \ge 20°$) hereafter called *typical AERONET-OC measurement conditions*.

Given these negligible differences, ρ_d can be confidently utilized to determine the sky-glint contributions to L_T.

Table 1. Values of the main parameters for the computation of the ρ-factors; g_{500} indicates the phase function asymmetry parameter at 500 nm.

Center-wavelength λ [nm]	340, 380, 400, 412, 440, 443, 490, 500, 510, 531, 532, 551, 560, 620, 667, 675, 681, 709, 779, 865, 870, 1020
Sun zenith θ_0 [°]	10, 20, 30, 40, 50, 60, 70, 80
Sun azimuth ϕ_0 [°]	0
Wind speed v_w [m s^{-1}]	0, 2, 4, 6, 8, 10
Aerosol optical depth at 560 nm, τ_a^{560}	0.05, 0.1, 0.2, 0.3, 0.4, 0.5
Tropospheric aerosol model (RH = 80 %)	Maritime (MA): $\alpha_{350-500} = 0.12$; $\alpha_{500-800} = 0.08$; $g_{500} = 0.77$ Mixed (MX): $\alpha_{350-500} = 0.93$; $\alpha_{500-800} = 1.06$; $g_{500} = 0.72$ Continental (CO): $\alpha_{350-500} = 1.13$; $\alpha_{500-800} = 1.45$; $g_{500} = 0.70$

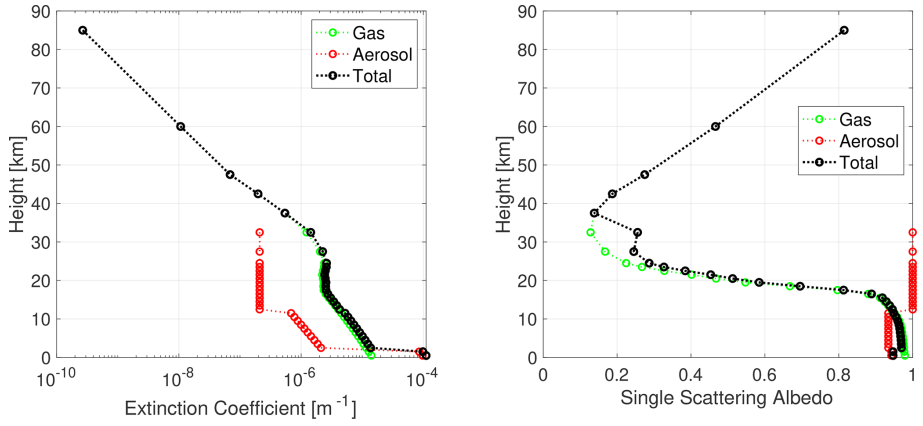


Figure 3. Vertical profile at 560 nm of extinction coefficient and single scattering albedo for gas molecules, aerosols, and their combination when adopting the MX tropospheric aerosol model and $\tau_a^{560} = 0.2$.

The newly computed ρ_d values are slightly lower than those used in Zibordi et al. (2025), with mean percent differences never exceeding −1.2 % for the typical AERONET-OC measurement conditions. The update in the vertical aerosol profile has a minimal impact on the computation of ρ_d, while the adoption of the AFGL gas molecule model is responsible for the overall slight decrease, with the largest differences occurring for clear atmospheres in the ultraviolet.

Even though not relevant for AERONET-OC processing, the revisions applied to the atmospheric model have a larger impact on ρ_T with a mean percent decrease up to −4.2 % across all cases, which narrows down to −1.1 % for typical AERONET-OC measurement conditions.

3 Results and discussion

Results are presented by first illustrating the main components of Eq. (3) – the diffuse sky-radiance and the water-surface reflectance matrices – followed by a detailed analysis of the ρ_T and ρ_d values and their dependence on environmental parameters.

Figure 5a displays the angular distribution of the diffuse sky radiance (i.e., matrix **L** for diffuse L_{sky}) at $\lambda = 560$ nm, for the MX aerosol model, $\tau_a^{560} = 0.2$, and $\theta_0 = 40°$. The additional plots of Fig. 5b–i illustrate the dependence of the diffuse sky radiance on sun elevation, wavelength, aerosol load and type. Under conditions characterized by reduced multiple scattering (low θ_0, long λ, low τ_a^{560}, and more forward-scattering aerosol), the angular distribution of the diffuse sky radiance shows a narrower peak near the sun-quad.

Examples of *water-surface reflectance matrices* **R** at 560 nm are given in Fig. 6, clearly depicting a consistent enlargement with wind speed of the portion of the sky-dome contributing to L_R.

3.1 Considerations on sun-glint contributions

The probability to sample the sun-quad – identified by (k_s, m_s) – is here expressed as $\mathbf{R}_{sq} = \frac{\mathbf{R}(k_s,m_s)}{\sum_k^{N_\theta}\sum_m^{N_\phi}\mathbf{R}(k,m)} \cdot 100$.

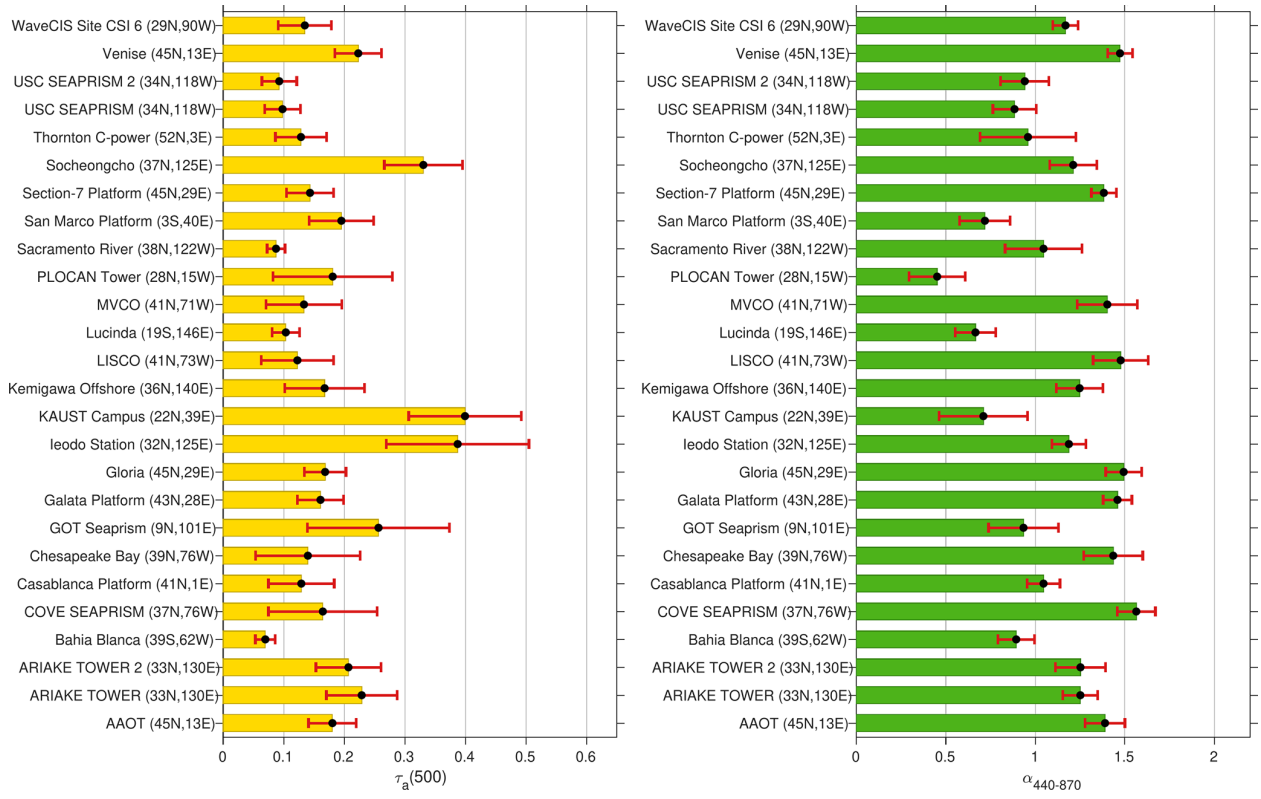


Figure 4. AERONET climatological aerosol optical data at reference AERONET-OC sites. The left and right panels display multi-annual yearly average values of τ_a^{500} and $\alpha_{440–870}$, respectively. Black dots indicate the mean values and red bars $\pm$ 1 standard deviation.

Representative values of $\mathbf{R}_{sq}$, together with their statistical uncertainty, are provided in Table 2 for $\lambda = 560$ nm and $\theta_0 = 40°$. Within the Monte Carlo (MC) statistical uncertainties, $\mathbf{R}_{sq}$ shows a strong increase with wind speed, yet remains within 0.005 % even for $v_w = 10\,m\,s^{-1}$. Nonetheless, plots of Fig. 7, which display the angular origin of direct and diffuse sky-radiance contributions to L_R (i.e., $L_R(k,m) = \mathbf{R}(k,m) \cdot \mathbf{L}(k,m)$), highlight how contributions to L_R from the sun-quad (i.e., the sun-glint $L_R(k_s,m_s) = \mathbf{R}(k_s,m_s) \cdot \mathbf{L}(k_s,m_s)$) are already significant for $v_w = 6\,m\,s^{-1}$, and how they become the most important contribution for $v_w = 8\,m\,s^{-1}$, as evidenced by the sun-quad being the brightest element in the figure.

These findings further underline the need to carefully apply quality-control procedures to filter out measurements affected by sun-glint contamination.

Since values of $\rho_D = \rho_T - \rho_d$ might be used to theoretically estimate sun-glint contributions to L_T, Fig. 8 presents ρ_D for the MX aerosol model and for representative wavelengths and aerosol loads. Results confirm that sun-glint contributions strongly increase with wind speed and with conditions favoring larger direct sky-radiance, i.e., for longer wavelengths, low aerosol optical depth and low solar zenith angles.

Notably, the most favorable measurement conditions intrinsically confirmed by AERONET-OC quality-controlled data (Zibordi et al., 2022) correspond to cases with negligible sun-glint contamination: low-to-mild wind speeds v_w tentatively not exceeding $4\,m\,s^{-1}$, and sun zenith angles θ_0 larger than approximately 20°.

3.2 Overall characterization of ρ_T and ρ_d factors

Assuming that quality-control procedures allow for removing measurements affected by sun-glint, the correction for surface perturbations in above-water radiometry can solely rely on ρ_d.

Nevertheless, the long-standing community-wide application of ρ-factors accounting for total sky-radiance contributions suggests the determination and provision of both ρ_T and ρ_d.

Full and conditional distributions of ρ_T are summarized in Fig. 9. The histogram distribution of ρ_T (displayed on a logarithmic scale in Fig. 9a) is extremely skewed, with a long tail of rare, yet extremely large values, corresponding to conditions of high wind speeds, low solar zenith angles, low aerosol loads and long wavelengths, as reflected in the largest right whiskers of the box plots of Fig. 9b–f.

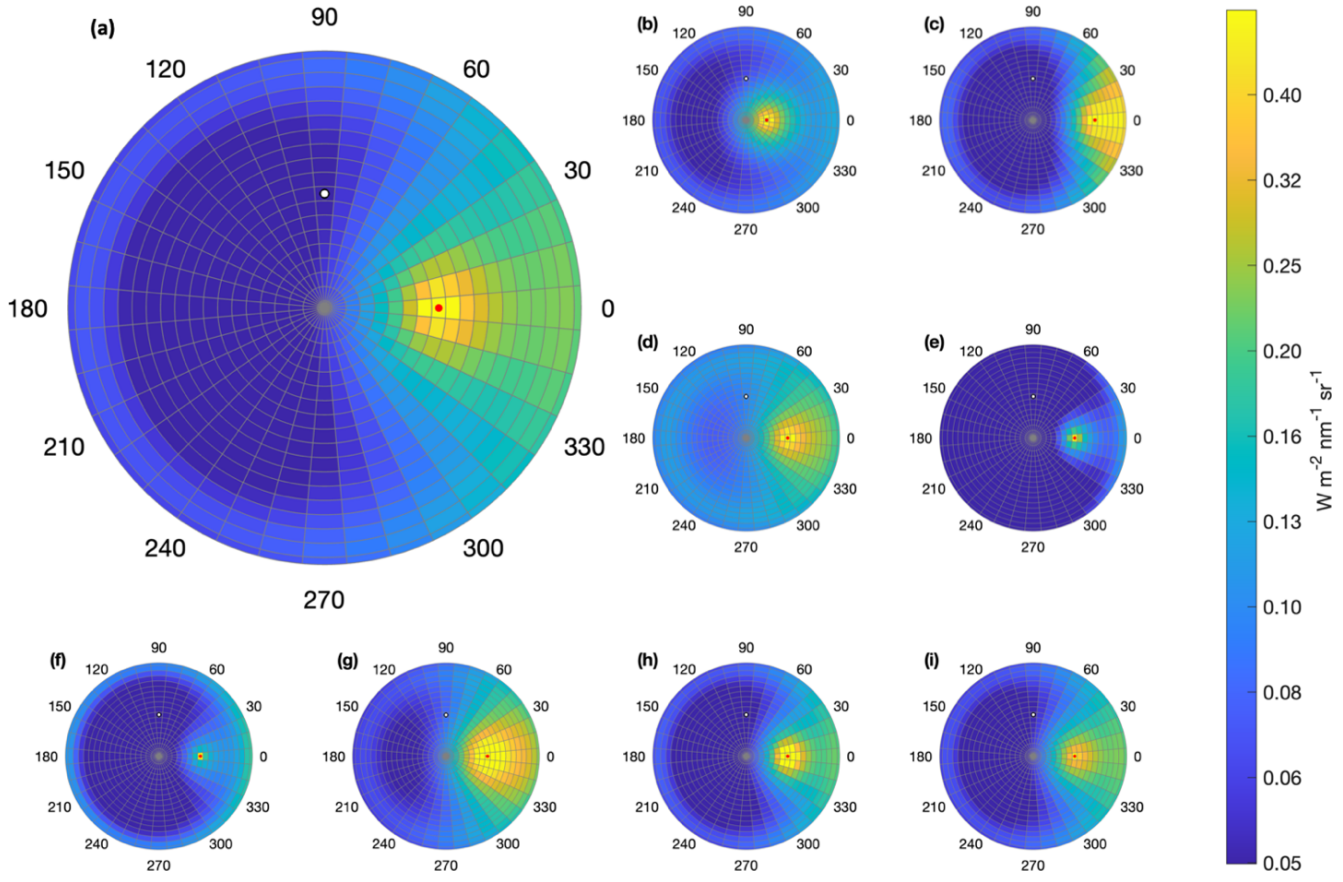


Figure 5. Angular distribution of the diffuse sky radiance **(a)** at 560 nm for the MX aerosol model with $\tau_a^{560} = 0.2$ and $\theta_0 = 40°$, and alternatively for **(b)** $\theta_0 = 20°$, **(c)** $\theta_0 = 60°$, **(d)** $\lambda = 412$ nm, **(e)** $\lambda = 865$ nm, **(f)** $\tau_a^{560} = 0.05$, **(g)** $\tau_a^{560} = 0.5$, **(h)** the MA tropospheric aerosol model, **(i)** the CO tropospheric aerosol model. The solar plane crosses the hemisphere from $\phi = 0°$ to $\phi = 180°$. The measurement plane crosses the hemisphere from $\phi = 90°$ to $\phi = 270°$. The red dot indicates the sun-quad; the white dot the L_i-quad.

Table 2. Probability $\mathbf{R}_{sq} \pm \sigma$ (in percent) of sampling the sun-quad for $\lambda = 560$ nm and $\theta_0 = 40°$.

v_w [m s^{-1}]	0	2	4	6	8	10
$\mathbf{R}_{sq}$	0.0	8.4×10^{-7}	1.6×10^{-5}	2.0×10^{-4}	1.4×10^{-3}	4.8×10^{-3}
σ	0.0	8.2×10^{-7}	4.5×10^{-6}	1.9×10^{-5}	3.8×10^{-5}	8.3×10^{-5}

These environmental conditions are associated with sun-glint contamination. Figure 9b additionally shows clearly separated box-plots for the lowest wind speeds.

Apart from the strong increase of ρ_T with wind speed and decreasing sun zenith angle, explained by sun-glint contamination, the plots further show a noticeable overall ρ_T decrease with increasing aerosol load (as a consequence of a more isotropic distribution of the sky-radiance) and an appreciable increase with wavelength (as a consequence of aerosol optical depth decrease).

When considering the sole diffuse sky-radiance contributions to water-surface reflection (Fig. 10), the histogram distribution of ρ_d (displayed on a linear scale in Fig. 10a) does not exhibit the long tail observed for ρ_T. The more symmetric distribution still shows well-separated box plots at low wind speeds, which increasingly overlap for larger v_w (Fig. 10b), confirming wind speed as the major driver of ρ_d variability. The box plots of Fig. 10c–f show how the overall dependence of ρ_d on θ_0, λ, and aerosol type and load, is considerably lower than that of ρ_T. Still noticeable is a slight increase in ρ_d median and interquartile range values for decreasing sun elevation, increasing wavelength, decreasing aerosol load and for the maritime aerosol.

The significant dependence of ρ_d on the wind speed motivated a detailed analysis for each discrete v_w value separately (see Sect. 3.3).

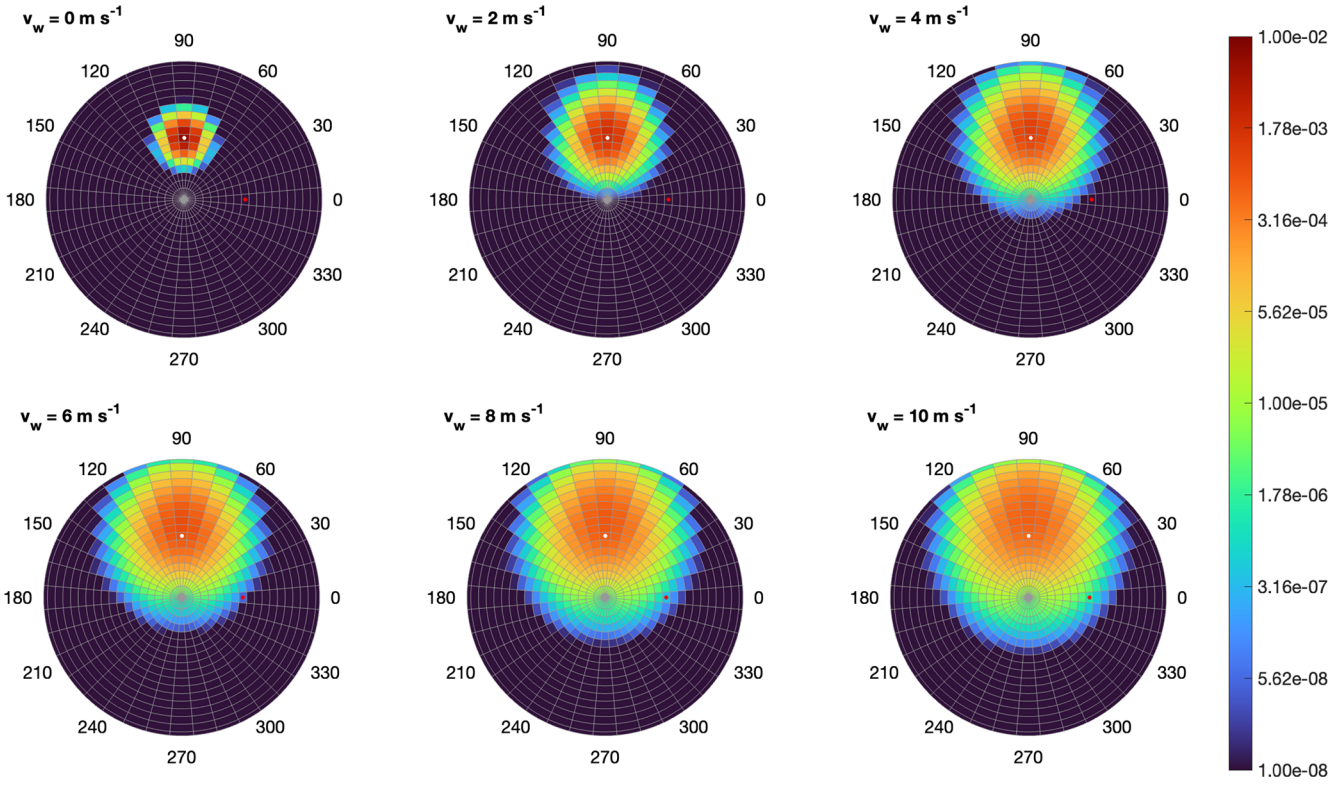


Figure 6. Water-surface reflectance matrix **R** determined at $\lambda = 560\,\text{nm}$ for v_w ranging from 0 to $10\,\text{m}\,\text{s}^{-1}$, at $2\,\text{m}\,\text{s}^{-1}$ increment. The solar plane crosses the hemisphere from $\phi = 0°$ to $\phi = 180°$. The measurement plane crosses the hemisphere from $\phi = 90°$ to $\phi = 270°$. The white dot indicates the L_i-quad; the red dot the sun-quad when $\theta_0 = 40°$. Results for $v_\text{w} = 0\,\text{m}\,\text{s}^{-1}$ are explained by the background term of Eq. (4).

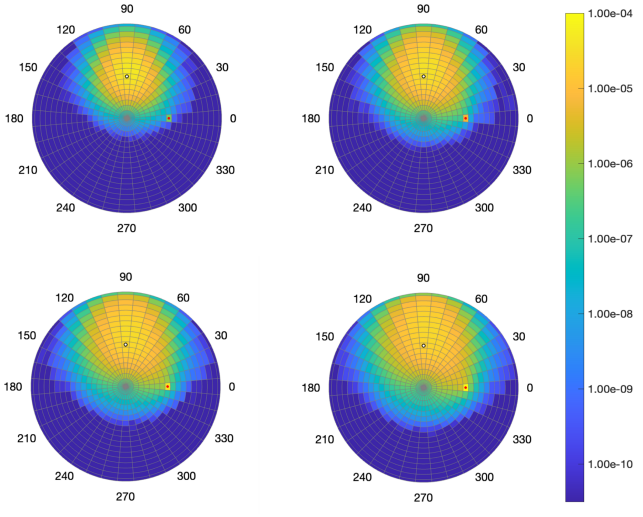


Figure 7. Angular distribution of the sky-dome origin of direct and diffuse radiance contributions to L_R (i.e., $L_\text{R}(k, m)$), as determined for the MX aerosol at 560 nm with $\theta_0 = 40°$ and (from top-left to bottom-right) $v_\text{w} = 4, 6, 8, 10\,\text{m}\,\text{s}^{-1}$. The red dot indicates the sun-quad. The white dot indicates the L_i-quad.

Examples of ρ_d values are given in Fig. 11 for the same simulation conditions applied to the ρ_D values plotted in Fig. 8 (note that the scale is one order of magnitude lower).

3.3 Detailed analysis of atmospheric and spectral dependences

In Bulgarelli et al. (2024), values of ρ_T were presented and discussed with a specific focus on spectral and atmospheric changes with respect to reference values ρ_T^REF computed at 551 nm for average climatological atmospheric conditions ($\tau_\text{a}^{560} = 0.2$ and MX aerosol model), i.e., the simulation conditions best matching those adopted for the computation of community ρ_T-factors by Mobley (1999). The analysis highlighted an overall variation of $\Delta\rho_\text{T} = \left(\frac{\rho_\text{T}}{\rho_\text{T}^\text{REF}} - 1\right) \cdot 100$ up to sixfold, narrowing drastically to within a few percent for the typical AERONET-OC measurement conditions.

The same analysis is here conducted on ρ_d, further noting that the selected spectral and atmospheric conditions (551 nm, $\tau_\text{a}^{560} = 0.2$, and MX aerosol model) correspond to ρ_d close to its global mean. For each v_w and θ_0, changes of ρ_d with respect to ${\rho_\text{d}}^\text{REF}$ are computed through the percent difference

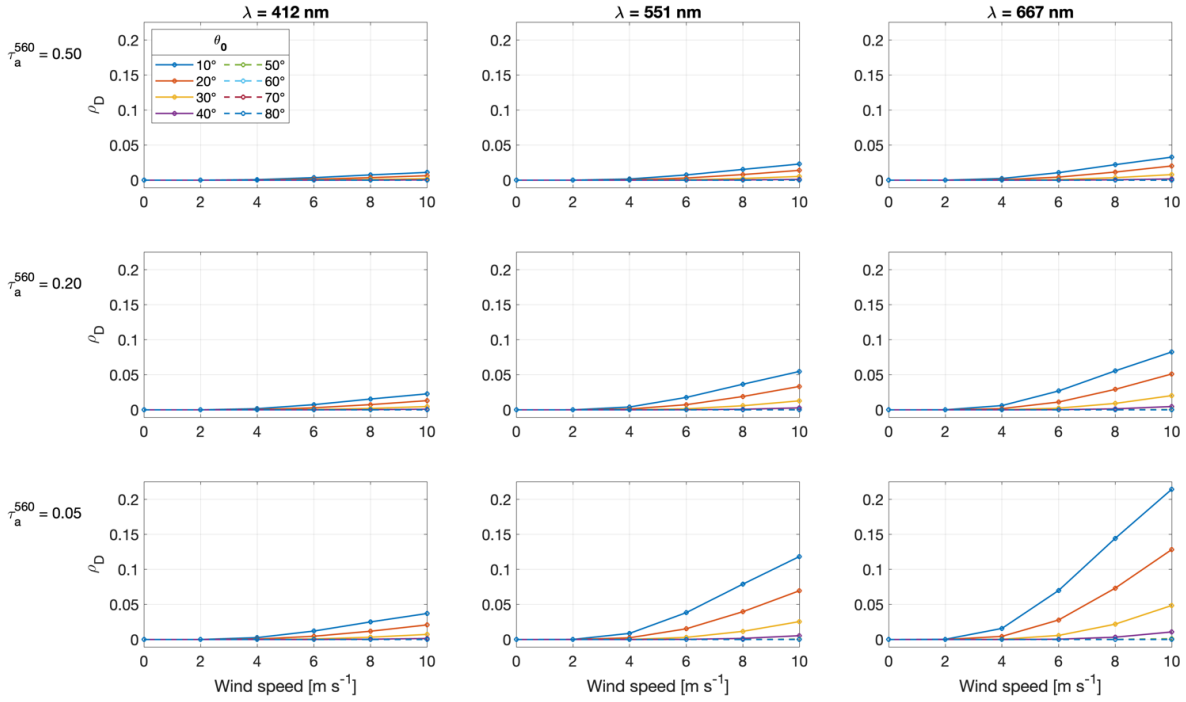


Figure 8. Plots of ρ_D as a function of wind speed for different values of θ_0. Results are for the MX aerosol model at representative wavelengths and for different values of τ_a^{560}.

$$\Delta\rho_d\left(\theta_0; v_w; \lambda; \tau_a^{560}; A\right) = \left(\frac{\rho_d\left(\theta_0; v_w; \lambda; \tau_a^{560}; A\right)}{\left(\rho_d^{REF}\left(\theta_0; v_w; \lambda = 551; \tau_a^{560} = 0.2; A = MX\right)\right)} - 1\right) \cdot 100, \quad (5)$$

where A stands for the aerosol type.

3.3.1 Dependence on the aerosol load

For reference aerosol type and wavelength, results of Fig. 12 indicate that when $v_w \leq 4\,m\,s^{-1}$, $\Delta\rho_d$ ranges from $-2.8\,\%$ to $+0.9\,\%$, confirming low sensitivity to the aerosol optical depth regardless of θ_0. Yet, for larger wind speeds, $\Delta\rho_d$ displays an appreciable decrease with τ_a^{560} that becomes more pronounced at high sun zenith angles. For extreme measurement conditions ($v_w = 10\,m\,s^{-1}$ and $\theta_0 = 80°$) $\Delta\rho_d$ ranges from $-7.5\,\%$ to $+4.0\,\%$ when τ_a^{560} decreases from 0.5 to 0.05.

As expected, the dependence of ρ_T on the aerosol load (not shown here) is consistently more pronounced when v_w exceeds $4\,m\,s^{-1}$, reaching $-36.9\,\%$ (for $\tau_a^{560} = 0.5$) and $+72.5\,\%$ (for $\tau_a^{560} = 0.05$) when $v_w = 10\,m\,s^{-1}$ and $\theta_0 = 10°$.

3.3.2 Spectral dependence

The spectral dependence of glint correction factors is induced by the spectral variation of both the atmospheric optical properties and, to a lesser extent, the water refractive index.

Figure 13 shows plots of $\Delta\rho_d$ for reference aerosol type and load. Results for $v_w = 0\,m\,s^{-1}$ highlight the influence essentially due to the spectral change of the water refractive index, which leads to a slight decrease of ρ_d with wavelength. Opposite is the effect of the optical depth: the spectral decrease of τ_a induces a spectral increase of ρ_d (in agreement with Sect. 3.3.1). This spectral dependence of ρ_d is more pronounced for high θ_0 and v_w: spectral values of $\Delta\rho_d$ vary between $-3.8\,\%$ and $+7.1\,\%$ for $v_w \leq 4\,m\,s^{-1}$, but within $-16.6\,\%$ and $+14.0\,\%$ for $\theta_0 = 80°$ and $v_w = 10\,m\,s^{-1}$.

As expected, the spectral dependence of ρ_T is consistently more pronounced for wind speeds higher than $4\,m\,s^{-1}$, reaching $-53.8\,\%$ (at 340 nm) and $+129.8\,\%$ (at 1020 nm) when $v_w = 10\,m\,s^{-1}$ and $\theta_0 = 10°$.

3.3.3 Dependence on the aerosol type

The optical properties of continental aerosols exhibit stronger spectral variations in comparison to those of mixed and maritime aerosols, while the phase function is less forward-peaked: this clearly affects the spectral dependence of ρ_d. Illustrative results are provided in Fig. 14 for pure maritime (MA) and pure continental (CO) aerosols with $\tau_a^{560} = 0.2$ and $v_w = 10\,m\,s^{-1}$. Although in both cases $\Delta\rho_d$ varies

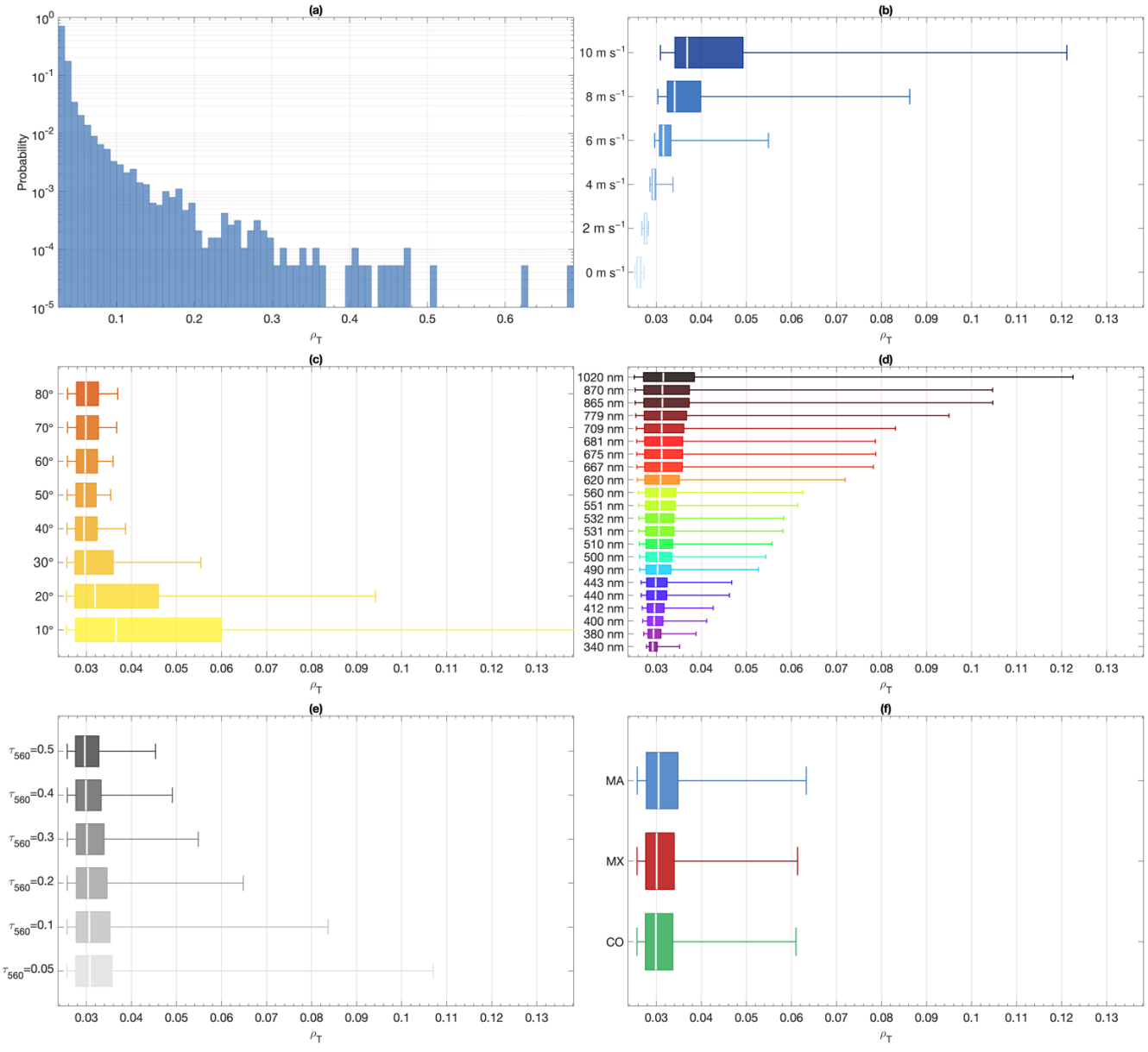


Figure 9. Panel **(a)** shows the histogram distribution of ρ_T on a logarithmic scale. The other panels display the box plots of ρ_T for different values of **(b)** wind speed v_w, **(c)** solar zenith angle θ_0, **(d)** wavelength λ, **(e)** aerosol optical depth τ_a^{560}, and **(f)** aerosol type, while marginalizing out all other parameters. In the box plots, the vertical white line indicates the median, the box extends over the interquartile range, while the whiskers extend to the 5th and 95th percentiles.

between −16.8 % and +15.3 %, $\Delta\rho_d$ shows a much lower dependence on θ_0 in the presence of maritime aerosol.

Remarkably, the sensitivity of ρ_T to the aerosol type is much higher, and exhibits values of $\Delta\rho_T$ varying between −56.7 % and +52.4 % for the maritime aerosol, and between −53.5 % and +175.1 % for the continental aerosol.

3.3.4 Overall spectral and atmospheric variability

The overall variability of ρ_d with respect to reference values (i.e., those determined from average climatological conditions at 551 nm) is summarized in the histogram distribution of Fig. 15a. Specifically, $\Delta\rho_d$ varies between −20.2 % and +19.3 %, with a mean of −0.5 % and a standard deviation of 3.9 %. Conversely, values of $\Delta\rho_T$ determined with respect to the reference conditions (best approaching those applied by Mobley, 1999), vary from −59.6 % to +687 %, with a mean of +2.7 % and a standard deviation of 31.0 %.

When restricting the analysis to typical AERONET-OC measurement conditions in the 400–709 nm spectral inter-

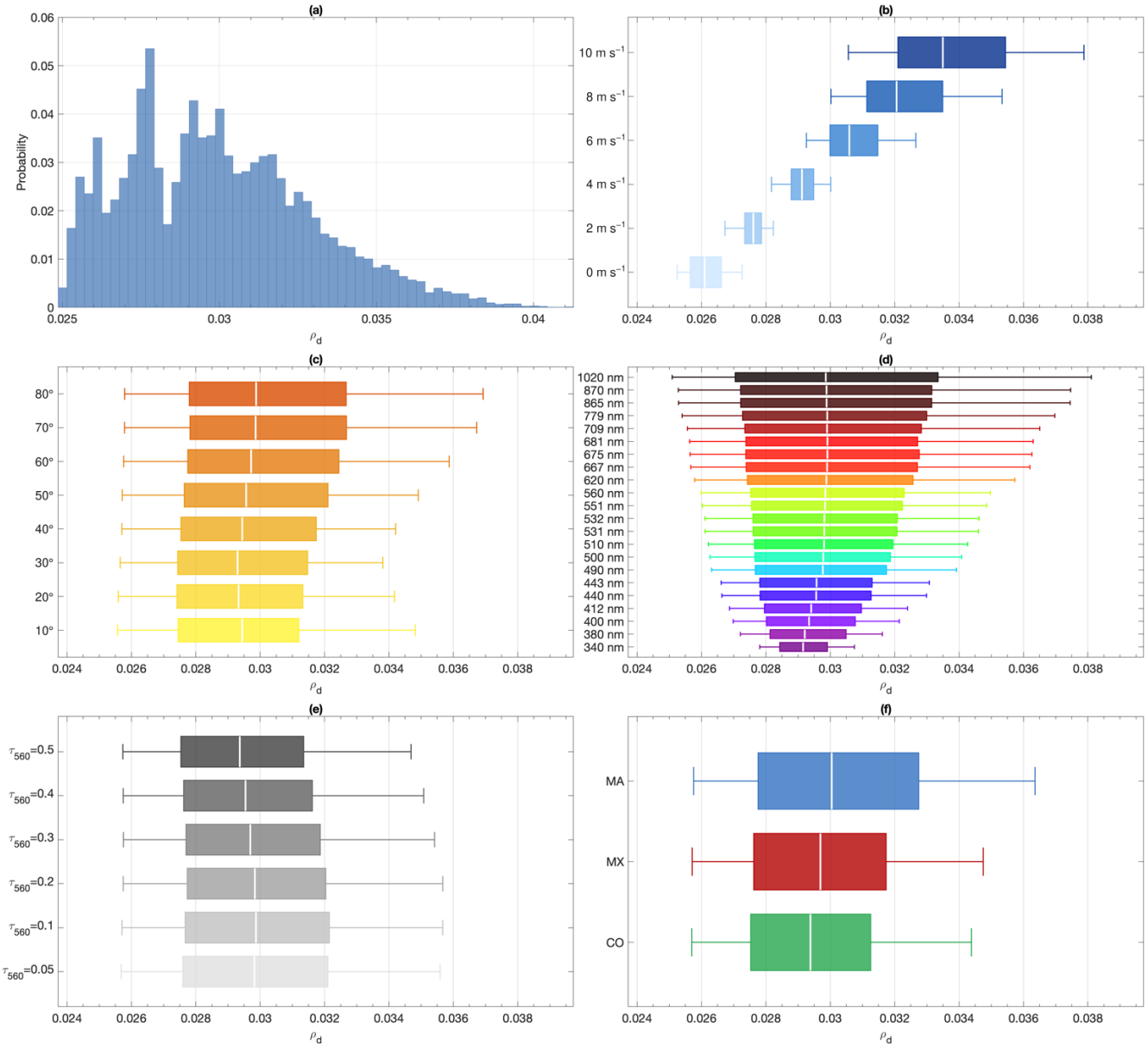


Figure 10. As in Fig. 9 but for ρ_d. Note that the scale of the distribution of ρ_d is now linear, and the x-axis range is considerably smaller.

val, the distribution of $\Delta\rho_d$ significantly narrows, exhibiting a standard deviation of 1.2 % (Fig. 15b).

3.4 Considerations on uncertainties

The weak dependence of ρ_d on τ_a^{560} (see Sect. 3.3.1) implies low ρ_d sensitivity to uncertainties in the aerosol load. Percent differences Δ_{τ_a} induced on ρ_d by an absolute uncertainty $u(\tau_a) = 0.02$ (Eck et al., 1999) are always below 1 %. Different is the case for ρ_T, where Δ_{τ_a} may reach 8 % for extreme measurement conditions defined by $v_w = 10\,\mathrm{m\,s^{-1}}$ and $\theta_0 = 10°$.

The variability of ρ_d with wind speed is more significant, and a realistic absolute uncertainty $u(v_w) = 2\,\mathrm{m\,s^{-1}}$ on v_w (De Vis et al., 2022; Cazzaniga and Zibordi, 2023) leads to more appreciable percent differences Δ_{v_w} on ρ_d, ranging from 4 % to 7 % at the reference conditions (see Fig. 16a). The more pronounced dependence of ρ_T on v_w implies a stronger sensitivity of ρ_T to uncertainties in the wind speed: for the same absolute uncertainty $u(v_w) = 2\,\mathrm{m\,s^{-1}}$, Δ_{v_w} on ρ_T reaches 46 % for the reference conditions (Fig. 16b).

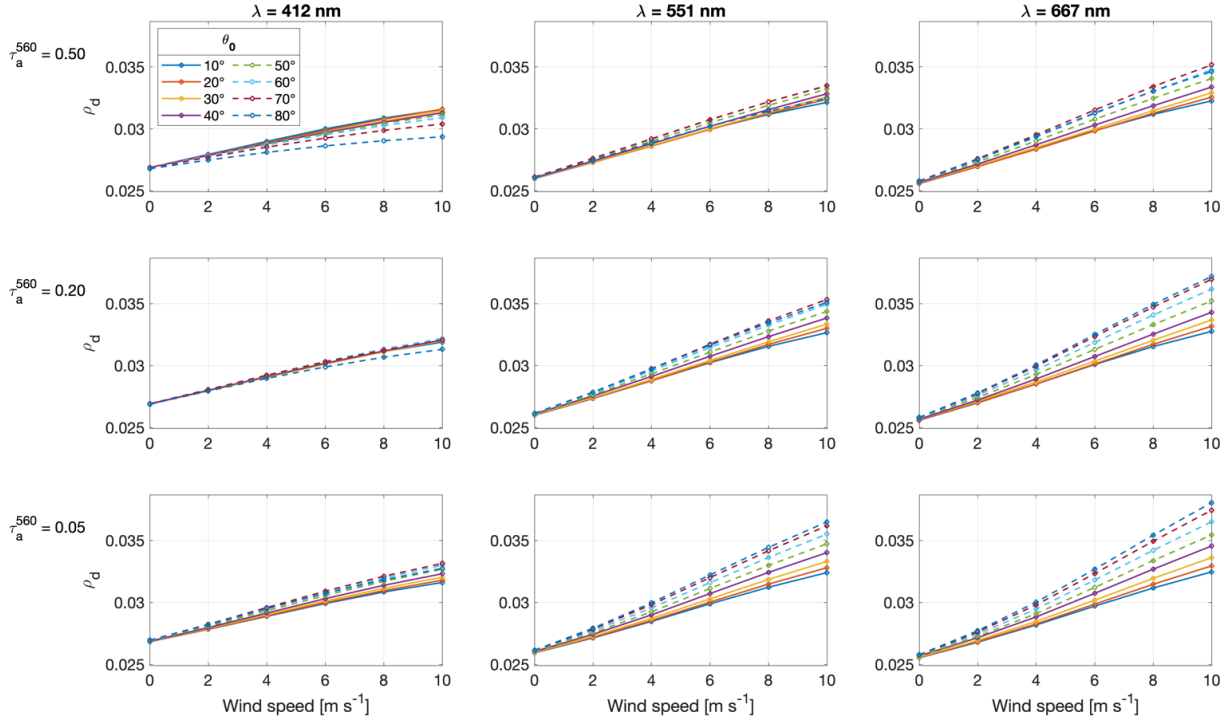


Figure 11. As in Fig. 8, but for ρ_d. Note that the scale is one order of magnitude lower.

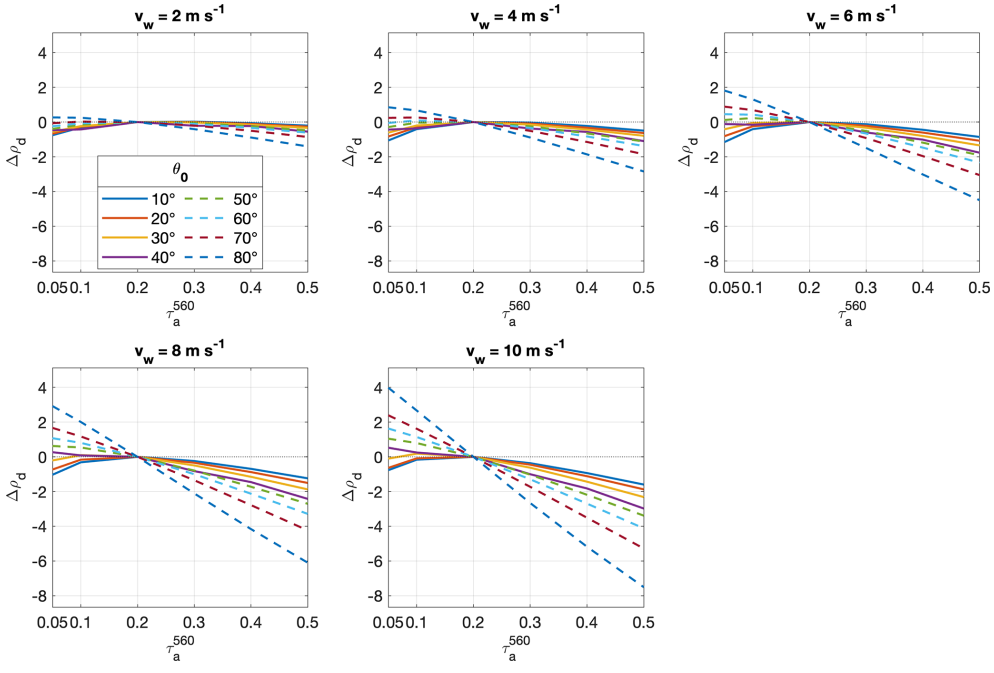


Figure 12. Values of $\Delta\rho_d$ (in percent) determined with respect to ρ_d^{REF} as a function of τ_a^{560} for different values of v_w and θ_0. Each panel refers to a different value of v_w.

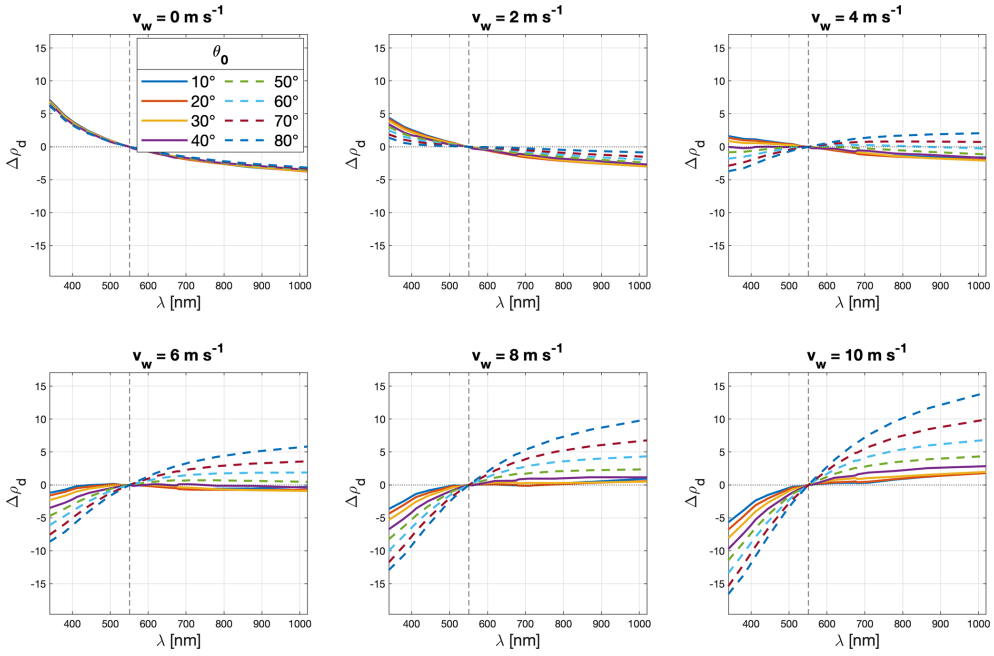


Figure 13. Values of $\Delta\rho_d$ (in percent) as a function of λ for the MX aerosol model with $\tau_a^{560} = 0.2$ and for different values of v_w and θ_0. Each panel refers to a specific value of v_w.

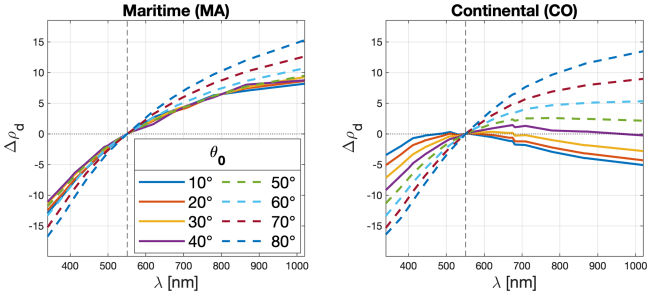


Figure 14. Spectral values of $\Delta\rho_d$ (in percent) for diverse aerosol types and θ_0 and for $\tau_a^{560} = 0.2$ and $v_w = 10\,m\,s^{-1}$.

4 Data availability

The newly computed spectral glint correction factors for above-water radiometric measurements are accessible at Zenodo (Bulgarelli et al., 2026; https://doi.org/10.5281/zenodo.20609990). The dataset is provided as a single HDF5 file (rho_factors.h5) consisting of two look-up tables: rho_dif containing the glint correction factors ρ_d computed using diffuse sky radiance, and rho_tot, the glint correction factors ρ_T computed using total sky radiance (diffuse and direct components). Values are tabulated as a function of tropospheric aerosol type (MA, CO, MX), aerosol optical depth at 560 nm (0.05–0.50), wavelength (340–1020 nm), solar zenith angle (10–80°), and wind speed (0–10 $m\,s^{-1}$). A README file documents the database structure and provides usage examples in Python.

5 Summary and conclusions

Glint correction factors ρ_T and ρ_d for the removal of water-surface reflection of total and diffuse sky-radiance in above-water radiometric measurements, respectively, were spectrally simulated in the 340–1020 nm region for a wide range of atmospheric, water-surface and illumination conditions typical of inland, coastal and open-ocean regions. Values of $\rho_D = \rho_T - \rho_d$ were additionally analyzed to provide physical insight into the origin and magnitude of sun-glint perturbations.

Computations were performed by adopting the AERONET-OC observation geometry supported by current measurement protocols, and relying on (i) the scalar FEM plane-parallel radiative transfer code in its SkyFEM configuration for the simulation of the angular distribution of the sky radiance impinging at the water surface and (ii) the MOX three-dimensional Monte Carlo code for the simulation of the water-surface reflecting properties under different wind conditions.

The impact of sun-glint perturbations was separately discussed, confirming its increase with wind speed and wavelength, and with decreasing solar zenith angle and aerosol load. Notably, it was also confirmed that AERONET-OC quality-controlled measurements, typically referring to $v_w \leq 4\,m\,s^{-1}$ and $\theta_0 \geq 20°$, inherently correspond to conditions of minor sun-glint contamination.

Given the long-standing application of ρ-factors accounting for total sky-radiance contributions, and, in turn, the advantage of solely considering the diffuse sky-radiance con-

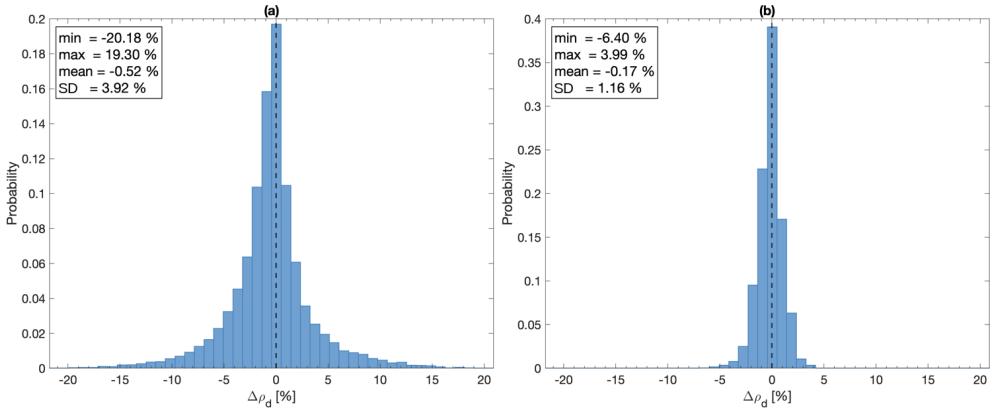


Figure 15. Normalized histograms of $\Delta\rho_d$ (in percent) for **(a)** overall data and **(b)** data characterized by $v_w \leq 4\,m\,s^{-1}$, $\theta_0 \geq 20°$ and λ within 400–709 nm. Statistical values refer to maximum (max), minimum (min), average (mean), and standard deviation (SD).

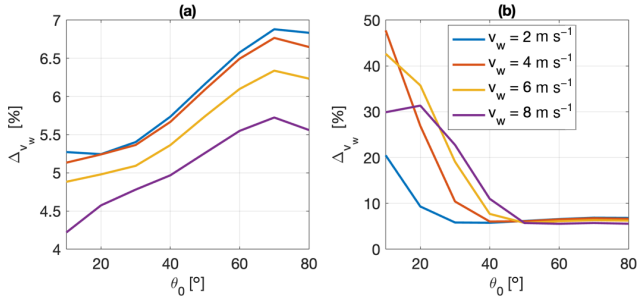


Figure 16. Percent differences Δ_{v_w} on **(a)** ρ_d and **(b)** ρ_T induced by an absolute uncertainty $u(v_w) = 2\,m\,s^{-1}$ on v_w at the reference conditions. Note that the scale is different.

tributions when quality-control procedures enable flagging measurements affected by sun-glint, both ρ_T and ρ_d values were presented and discussed.

The comparative analysis of ρ_T and ρ_d data highlighted (i) an extremely skewed distribution of ρ_T (due to sun-glint) with a strong dependence on simulation parameters such as wind speed and solar zenith angle; (ii) a considerably narrower distribution of ρ_d with a more regular shape still exhibiting a significant dependence on wind speed, but an overall lower dependence on the other simulation parameters.

The remarkable dependence of ρ_d on wind speed motivated a further analysis at discrete v_w values. Specifically, spectral and atmospheric changes of ρ_d were analyzed with respect to reference values at 551 nm for average atmospheric conditions, defined by the columnar Ångström exponent $\alpha^{col}_{440–870} = 1.08$ and aerosol optical depth $\tau_a^{560} = 0.2$. These reference parameters best correspond to those adopted by Mobley (1999) for the simulation of the community ρ_T-factors, and to cases around which mean ρ_d values occur. The analysis showed low sensitivity of ρ_d to atmospheric optical properties, with a slight decrease with increasing aerosol load. Conversely, results showed a slight spectral decrease of ρ_d in the absence of wind, and a more consistent spectral increase with v_w. For reference aerosol load and type, a maximum spectral variation from −16.6 % to +14.0 % was shown for $\theta_0 = 80°$ and $v_w = 10\,m\,s^{-1}$.

Overall results indicated changes of ρ_d with respect to reference values distributed around −0.5 % with a standard deviation of 3.9 %. The standard deviation was shown to drop to 1.2 % for typical AERONET-OC observation conditions in the 400–709 nm spectral interval. Positive changes were observed for pure maritime aerosol and longer wavelengths, while negative changes were shown for optically thicker atmospheres, pure continental aerosol and shorter wavelengths.

Evident were the much larger changes of ρ_T with respect to reference values, ranging from −59.6 % to +687 %, with a mean of +2.7 % and a standard deviation of 31.0 %.

This has clear implications for the sensitivity of glint correction factors to uncertainties in input parameters. While ρ_T shows high sensitivity to uncertainties in wind speed and/or aerosol optical depth, values of ρ_d exhibit relative stability.

Based on results from Zibordi et al. (2025), the impact of the newly computed ρ_d in the determination of L_w is expected to be significant.

Appendix A

List of main mathematical symbols used in the manuscript.

Symbol	Definition
λ	wavelength
θ	sensor angle of view with respect to nadir
ϕ	azimuth angle between solar and measurement planes
FOV	sensor Field-Of-View
θ_0	sun zenith angle
ϕ_0	sun azimuth angle
L_w	water-leaving radiance
L_T	total radiance measured by the in situ above-water sensor when observing the water
L_i	sky radiance measured by the in situ above-water sensor when observing the sky
L_R	radiance reflected by the water surface
L_{sky}	simulated downwelling sky radiance
r	probability density
ρ	glint correction factor
ρ_T	glint correction factor accounting for the total (direct and diffuse) sky-radiance L_{sky}
ρ_d	glint correction factor accounting for the sole diffuse component of L_{sky}
$\rho_{\tilde{sq}}$	glint correction factor computed by masking the sun-quad
R	water-surface reflectance matrix
L	sky-radiance matrix
τ_a	aerosol optical depth
τ_a^λ	aerosol optical depth at the λ wavelengths
$\alpha_{350–500}$	Ångström exponent for the 350–500 nm range
$\alpha_{500–800}$	Ångström exponent for the 500–800 nm range
$\alpha^{col}_{440–870}$	columnar Ångström exponent for the 440–870 nm range
g_{500}	phase function asymmetry parameter at 500 nm
RH	relative humidity
MA	tropospheric Maritime aerosol
MX	tropospheric Mixed aerosol
CO	tropospheric Continental aerosol
v_w	wind speed
σ^2	variance of the wave-slope distribution

Author contributions. BB, GZ and DD contributed to the conceptualization of the study. BB performed the formal data analysis and prepared the original draft. BB and DD contributed to data curation; BB, DD and TK to the software development. All authors contributed to the review and editing.

Competing interests. The contact author has declared that none of the authors has any competing interests.

Disclaimer. Publisher's note: Copernicus Publications remains neutral with regard to jurisdictional claims made in the text, published maps, institutional affiliations, or any other geographical representation in this paper. The authors bear the ultimate responsibility for providing appropriate place names. Views expressed in the text are those of the authors and do not necessarily reflect the views of the publisher.

Financial support. G. Zibordi was supported by the National Aeronautics and Space Administration through the Southeastern Universities Research Association, Goddard Earth Sciences Technology and Research II Award, grant 80NSSC22M0083. B. Bulgarelli was supported by the European Commission Directorate-General Joint Research Centre (JRC), and the Directorate-General for Defence Industry and Space (DEFIS). D. D'Alimonte and T. Kajiyama were supported by the JRC, contract 939934.

Review statement. This paper was edited by Salvatore Marullo and reviewed by three anonymous referees.

References

Anderson, G. P., Clough, S. A., Kneizys, F. X., Chetwynd, J. H., and Shettle, E. P.: AFGL Atmospheric Constituent Profiles (0–120 km), AFGL-TR-86-0110, Air Force Geophysics Laboratory, Hanscom AFB, MA, https://www.researchgate.net/profile/Eric-Shettle/publication/235054307_AFGL_Atmospheric_Constituent_Profiles_0120km/links/00b7d5261849c835c1000000/AFGL-Atmospheric-Constituent-Profiles-0120km.pdf (last access: 3 November 2026), 1986.

Ångström, A.: Techniques of determining the turbidity of the atmosphere, Tellus, 13, 214–223, https://doi.org/10.1111/j.2153-3490.1961.tb00078.x, 1961.

Berk, A., Anderson, G. P., Acharya, P. K., Bernstein, L. S., Muratov, L., Lee, J., Fox, M., Adler-Golden, S. M., Chetwynd, J. H., Hoke, M. L., Lockwood, R. B., Gardner, J. A., Cooley, T. W., Borel, C. C., Lewis, P. E., and Shettle, E. P.: MODTRAN5: 2006 update, Proc. SPIE 6233, Algorithms and Technologies for Multispectral, Hyperspectral, and Ultraspectral Imagery XII, 62331F, https://doi.org/10.1117/12.665077, 2006.

Bulgarelli, B.: Advanced Radiative Transfer Models for the simulation of in situ and satellite ocean color data (ARTEMIS-OC): the Finite Element Method (FEM) numerical code, JRC Technical Report JRC135763, Publications Office of the European Union, Luxembourg, https://doi.org/10.2760/30247, 2024.

Bulgarelli, B. and Doyle, J. P.: Comparison between numerical models for radiative transfer simulation in the atmosphere–ocean system, J. Quant. Spectrosc. Ra., 86, 315–334, https://doi.org/10.1016/j.jqsrt.2003.08.009, 2004.

Bulgarelli, B., Kisselev, V. B., and Roberti, L.: Radiative transfer in the atmosphere-ocean system: the finite-element method, Appl. Optics, 38, 1530–1542, https://doi.org/10.1364/AO.38.001530, 1999.

Bulgarelli, B., Zibordi, G., and Berthon, J.-F.: Measured and modeled radiometric quantities in coastal wa-

ters: toward a closure, Appl. Optics, 42, 5365–5381, https://doi.org/10.1364/AO.42.005365, 2003.

Bulgarelli, B., D'Alimonte, D., Zibordi, G., and Kajiyama, T.: Sea-surface reflectance factor: spectral and atmospheric dependence, Ocean Optics XXVI, Abstract 615, Oral Session 7, 5 October 2022, Quy Nhon, Vietnam, https://2022.oceanopticsconference.org/abstract-bulgarelli/ (last access: 3 November 2026), 2022.

Bulgarelli, B., D'Alimonte, D., Zibordi, G., and Kajiyama, T.: AERONET-OC reference measurements to assess Earth Observation data: towards a revised data reduction protocol, EUR 40036, JRC139003, Publications Office of the European Union, Luxembourg, https://doi.org/10.2760/2707793, 2024.

Bulgarelli, B., D'Alimonte, D., Zibordi, G., and Kajiyama, T.: Spectral correction factors for the removal of glint perturbations in above-water radiometry, Zenodo [data set], https://doi.org/10.5281/zenodo.20609990, 2026.

Cazzaniga, I. and Zibordi, G.: AERONET-OC LWN uncertainties: revisited, J. Atmos. Ocean. Tech., 40, 411–425, https://doi.org/10.1175/JTECH-D-22-0061.1, 2023.

Chami, M., Lafrance, B., Fougnie, B., Chowdhary, J., Harmel, T., and Waquet, F.: OSOAA: a vector radiative transfer model of coupled atmosphere-ocean system for a rough sea surface application to the estimates of the directional variations of the water leaving reflectance to better process multi-angular satellite data over the ocean, Opt. Express, 23, 27829–27852, https://doi.org/10.1364/OE.23.027829, 2015.

Cox, C. and Munk, W.: Measurement of the roughness of the sea surface from photographs of the sun's glitter, J. Opt. Soc. Am., 44, 838–850, https://doi.org/10.1364/JOSA.44.000838, 1954.

D'Alimonte, D., Zibordi, G., Kajiyama, T., and Cunha, J. C.: Monte Carlo code for high spatial resolution ocean color simulations, Appl. Optics, 49, 4936–4950, https://doi.org/10.1364/AO.49.004936, 2010.

D'Alimonte, D., Kajiyama, T., Zibordi, G., and Bulgarelli, B.: Sea-surface reflectance factor: replicability of computed values, Opt. Express, 29, 25217–25231, https://doi.org/10.1364/OE.424768, 2021.

D'Alimonte, D., Bulgarelli, B., Kajiyama, T., and Zibordi, G.: Theoretical assessment of structure perturbations in above-water radiometry, Opt. Express, 34, 25549–25577, https://doi.org/10.1364/OE.582648, 2026.

De Vis, P., Mélin, F., Hunt, S. E., Morrone, R., Sinclair, M., and Bell, B.: Ancillary data uncertainties within the SeaDAS uncertainty budget for ocean colour retrievals, Remote Sens., 14, 497, https://doi.org/10.3390/rs14030497, 2022.

Eck, T. F., Holben, B. N., Reid, J. S., Dubovik, O., Smirnov, A., O'Neill, N. T., Slutsker, I., and Kinne, S.: Wavelength dependence of the optical depth of biomass burning, urban, and desert dust aerosols, J. Geophys. Res.-Atmos., 104, 31333–31349, https://doi.org/10.1029/1999JD900923, 1999.

Elfouhaily, T., Chapron, B., Katsaros, K., and Vandemark, D.: A unified directional spectrum for long and short wind-driven waves, J. Geophys. Res., 102, 15781–15796, https://doi.org/10.1029/97JC00467, 1997.

Gilerson, A., Carrizo, C., Foster, R., and Harmel, T.: Variability of the reflectance coefficient of skylight from the ocean surface and its implications to ocean color, Opt. Express, 26, 9615–9633, https://doi.org/10.1364/OE.26.009615, 2018.

Harmel, T.: Apparent surface-to-sky radiance ratio of natural waters including polarization and aerosol effects: implications for above-water radiometry, Front. Remote Sens., 4, 1307976, https://doi.org/10.3389/frsen.2023.1307976, 2023.

Harrison, A. W. and Coombes, C. A.: An opaque cloud cover model of sky short wavelength radiance, Sol. Energy, 41, 387–392, https://doi.org/10.1016/0038-092X(88)90035-7, 1988.

Hess, M., Koepke, P., and Schult, I.: Optical properties of aerosols and clouds: the software package OPAC, B. Am. Meteorol. Soc., 79, 831–844, https://doi.org/10.1175/1520-0477(1998)079<0831:OPOAAC>2.0.CO;2, 1998.

Holben, B. N., Eck, T. F., Slutsker, I., Tanré, D., Buis, J. P., Setzer, A., Vermote, E., Reagan, J. A., Kaufman, Y. J., Nakajima, T., Lavenu, F., Jankowiak, I., and Smirnov, A.: AERONET – a federated instrument network and data archive for aerosol characterization, Remote Sens. Environ., 66, 1–16, https://doi.org/10.1016/S0034-4257(98)00031-5, 1998.

IOCCG: IOCCG Protocol Series. Protocols for Satellite Ocean Colour Data Validation: In Situ Optical Radiometry, IOCCG Ocean Optics and Biogeochemistry Protocols for Satellite Ocean Colour Sensor Validation, Zibordi, G., Voss, K. J., Johnson, B. C., and Mueller, J. L., Volume 3.0, IOCCG, Dartmouth, NS, Canada, https://ioccg.org/wp-content/uploads/2019/12/protocols-insitu-optical-radiometry-v3.0.pdf (last access: 1 November 2026), 2019.

Kajiyama, T., D'Alimonte, D., and Cunha, J. C.: A high-performance computing framework for Monte Carlo ocean color simulations, Concurr. Comp.-Pract. E., 29, e3860, https://doi.org/10.1002/cpe.3860, 2016.

Kisselev, V. B., Roberti, L., and Perona, G.: Finite-element algorithm for radiative transfer in vertically inhomogeneous media: numerical scheme and applications, Appl. Optics, 34, 8460–8471, https://doi.org/10.1364/AO.34.008460, 1995.

Lee, Z., Ahn, Y.-H., Mobley, C., and Arnone, R.: Removal of surface-reflected light for the measurement of remote-sensing reflectance from an above-surface platform, Opt. Express, 18, 26313–26324, https://doi.org/10.1364/OE.18.026313, 2010.

Mobley, C. D.: Light and Water: Radiative Transfer in Natural Waters, Academic Press, San Diego, 592 pp., https://oceanopticsbook.info/packages/iws_l2h/conversion/files/LightandWater.zip (last access: 3 November 2026), 1994.

Mobley, C. D.: Estimation of the remote-sensing reflectance from above-surface measurements, Appl. Optics, 38, 7442–7455, https://doi.org/10.1364/AO.38.007442, 1999.

Mobley, C. D.: Polarized reflectance and transmittance properties of windblown sea surfaces, Appl. Optics, 54, 4828–4849, https://doi.org/10.1364/AO.54.004828, 2015.

Sciuto, P., Zibordi, G., Bulgarelli, B., Talone, M., and Berthon, J. F.: UAV-based system for hyperspectral above-water radiometry, J. Atmos. Ocean. Tech., 43, 761–770, https://doi.org/10.1175/JTECH-D-26-0006.1, 2026.

Smirnov, A., Holben, B. N., Slutsker, I., Giles, D. M., McClain, C. R., Eck, T. F., Sakerin, S. M., Macke, A., Croot, P., Zibordi, G., Quinn, P. K., Sciare, J., Kinne, S., Harvey, M., Smyth, T. J., Piketh, S., Zielinski, T., Proshutinsky, A., Goes, J. I., Nelson, N. B., Larouche, P., Radionov, V. F., Goloub, P., Moorthy, K. K., Matarrese, R., Robertson, E. J., and Jourdin, F.: Maritime Aerosol Network as a component

of Aerosol Robotic Network, J. Geophys. Res.-Atmos., 114, D06204, https://doi.org/10.1029/2008JD011257, 2009.

Thuillier, G., Hersé, M., Labs, D., Foujols, T., Peetermans, W., Gillotay, D., Simon, P. C., and Mandel, H.: The solar spectral irradiance from 200 to 2400 nm as measured by the SOLSPEC spectrometer from the ATLAS and EURECA missions, Sol. Phys., 214, 1–22, https://doi.org/10.1023/A:1024048429145, 2003.

Tilstone, G. H., Jordan, T. M., Aurin, D., Białek, A., Deru, A., Ramsay, A., Hieronymi, M., Dall'Olmo, G., Ligi, M., Kovach, C., Ansko, I., Ondrusek, M., Vabson, V., Zibordi, G., Gossn, J., Kwiatkowska, E., and Vendt, R.: Radiometric field intercomparison of fiducial reference measurements using an open source community processor, Opt. Express, 33, 15756–15781, https://doi.org/10.1364/OE.551042, 2025.

Zhang, X., He, S., Shabani, A., Zhai, P.-W., and Du, K.: Spectral sea surface reflectance of skylight, Opt. Express, 25, A1–A13, https://doi.org/10.1364/OE.25.0000A1, 2017.

Zibordi, G.: Experimental evaluation of theoretical sea surface reflectance factors relevant to above-water radiometry, Opt. Express, 24, A446–A459, https://doi.org/10.1364/OE.24.00A446, 2016.

Zibordi, G. and Voss, K. J.: In situ optical radiometry in the visible and near infrared, in: Experimental Methods in the Physical Sciences, Vol. 47, 247–304, Academic Press, https://doi.org/10.1016/B978-0-12-417011-7.00010-6, 2014.

Zibordi, G., Mélin, F., Berthon, J.-F., Holben, B., Slutsker, I., Giles, D., D'Alimonte, D., Vandemark, D., Feng, H., Schuster, G., Fabbri, B. E., Kaitala, S., and Seppälä, J.: AERONET-OC: a network for the validation of ocean color primary products, J. Atmos. Ocean. Tech., 26, 1634–1651, https://doi.org/10.1175/2009JTECHO654.1, 2009.

Zibordi, G., Holben, B. N., Talone, M., D'Alimonte, D., Slutsker, I., Giles, D. M., and Sorokin, M. G.: Advances in the ocean color component of the Aerosol Robotic Network (AERONET-OC), J. Atmos. Ocean. Tech., 38, 725–746, https://doi.org/10.1175/JTECH-D-20-0085.1, 2021.

Zibordi, G., D'Alimonte, D., and Kajiyama, T.: Automated quality control of AERONET-OC LWN data, J. Atmos. Ocean. Tech., 39, 1961–1972, https://doi.org/10.1175/JTECH-D-22-0029.1, 2022.

Zibordi, G., D'Alimonte, D., Bulgarelli, B., Kajiyama, T., and Slutsker, I.: On the impact of alternative processing on AERONET-OC L_WN, J. Atmos. Ocean. Tech., 42, 1661–1674, https://doi.org/10.1175/JTECH-D-25-0038.1, 2025.